Extraction of Tsunami-Flooded Areas and Damaged Buildings in the 2011 Tohoku-Oki Earthquake from TerraSAR-X Intensity Images

Wen Liu,[a)] Fumio Yamazaki,[a)] M.EERI, Hideomi Gokon,[b)] and Shun-ichi Koshimura[b)]

The Tohoku earthquake of 11 March 2011 caused very large tsunamis and widespread devastation. Various high-resolution satellites captured details of affected areas and were utilized in emergency response. In this study, high-resolution pre- and post-event TerraSAR-X intensity images were used to identify tsunami-flooded areas and damaged buildings. Since water surface generally shows very little backscatter, flooded areas could be extracted by the difference of backscattering coefficients between the pre- and post-event images. Impacted buildings were detected by calculating the difference and correlation coefficient within the outline of each building. The damage estimates were compared with visual interpretation results, which suggest that the overall accuracy of the proposed method for flooded areas was 80%, and for damaged buildings was 94%. Since the proposed half-automated method takes less processing time and is applicable to various cases, it is expected to provide quick and useful information in emergency management. [DOI: 10.1193/1.4000120]

INTRODUCTION

The Tohoku earthquake on 11 March 2011 was the most powerful earthquake to hit Japan since modern recordkeeping began in 1900. The epicenter was located at 38.322°N, 142.369° E, at a depth of about 32 km. The earthquake triggered extremely high tsunamis of up to 40.5 m run-up in Miyako, Iwate Prefecture, and caused a huge loss of human lives and destruction of infrastructure. The tsunami height was far more extensive than the 2004 Indian Ocean mega-tsunami (Geist et al. 2006). According to the Geospatial Information Authority of Japan (GSI), areas totaling approximately 561 km^2 were flooded by tsunamis following the earthquake (GSI 2011). Due to this huge tsunami, about 129,000 residential buildings were washed away or collapsed. Thus, the extraction of flooded areas and damaged buildings is an important issue for this earthquake. The earthquake resulted from a thrust fault on the subduction zone plate boundary between the Pacific and North American plates. According to the GPS Earth Observation Network System (GEONET) operated by GSI in Japan, crustal movements exceeded 5.3 m horizontally and 1.2 m vertically over the wide areas of Tohoku region.

[a)] Graduate School of Engineering, Chiba University, 1-33 Yayoi-cho, Inage-ku, Chiba 163-8522, Japan
[b)] International Research Institute of Disaster Science, Tohoku University, 6-6-11-1104 Aoba, Aramaki, Aoba-ku, Sendai, 980-8579 Japan

Remote sensing has been recognized as an efficient tool to monitor a wide range of geo-physical events. Information from satellite altimetry has been used to develop high-resolution grids for pre-event planning (Mitsoudis et al. 2012). Although optical images can easily capture detailed ground surface information, the approach is limited by weather conditions. In contrast, synthetic aperture radar (SAR) sensing is independent of weather and daylight conditions, and thus more suitable for mapping damaged areas reliably and promptly. Due to remarkable improvements in radar sensors, high-resolution COSMO-SkyMed and Terra-SAR-X (TSX) SAR images are possible with ground resolution of 1 m to 5 m, providing detailed surface information.

As a preamble, Fritz et al. (2012) used high-resolution LIDAR to measure overland flow velocities in Kesennuma Bay through motion estimation from eyewitness videos. Here we focus on imaging radar for operational use in damage detection. Several different detection approaches were previously used for the derivation of flooding areas. Active contour models derived from a single SAR image (Horritt et al. 1999) gained popularity as a means of finding smooth water boundaries using tone and texture information. These algorithms were used in flood-boundary delineation by Ahtonen et al. (2002) and Matgen et al. (2007). From multi-temporal images, Heremans et al. (2003) detected flooded areas from ENVISAT/ASAR images using an amplitude-based method. Geudtner et al. (1996) and Dellepiane et al. (2000) monitored flooding from C-band SAR interferometry by coherence-based techniques. Due to the sensibility of X-band for fine reliefs and the high spatial resolution of the TSX sensor, TSX images can distinguish flooded areas more correctly. However, interferometry using X-band SAR can only be applied over limited regions (urbanized areas) with short periods due to the strong phase decorrelation caused by the short wavelength.

SAR images have also been used in interferometric analysis to investigate damage to buildings (Ito et al. 2000, Yonezawa and Takeuchi 2001). Matsuoka and Yamazaki (2004) performed a feasibility study on backscattering characteristics of damaged areas in the 1995 Kobe, Japan, earthquake and developed an automated method to detect hard-hit areas using ERS/SAR intensity images. The proposed method has also been applied to Envisat/ASAR images in the 2003 Bam, Iran, earthquake (Matsuoka and Yamazaki 2005). These studies focus on detecting damaged buildings on a block unit. Recently, several studies have attempted to detect damage at the scale of a building unit, using both high-resolution optical and SAR images (Brunner et al. 2010, Wang and Jin 2012). However, these studies still need the high-resolution optical images for supporting. Dell'Acqua and Gamba (2012) have made a summary of these methods for earthquake damage assessment.

In this study, we tried to identify both flooded areas and damaged buildings following the 2011 Tohoku tsunami only from multi-temporal TSX intensity images, and develop a simple approach for quick emergency response. We discuss in detail the different steps from pre-processing to noise reduction to allow for reliable identification. Flooded areas were identified by reduced backscattering intensity, and the parameters used were evaluated through comparison with optical images. A GIS map was then used to identify individual damaged buildings within the flooded areas (Gokon and Koshimura 2012). Finally, we assessed the accuracy of the proposed method through comparison with this GIS map.

SAR INTENSITY DATA AND PREPROCESSING

This study focuses on the coastal zone of Tohoku, Japan, shown in Figure 1a, which was most severely affected in the 2011 Tohoku earthquake. Three TerraSAR-X images taken before and after the earthquake (shown in Figure 1b–e) were used to distinguish flooded areas and damaged buildings. The pre-event image was taken on 21 October 2010 (UTC) with 37.3° incident angle, and two post-event images were taken on 13 March (two days after the earthquake) and 24 March 2011 with the same incidence angle at the center of the images. Those images were captured with HH polarization in a descending path. The images were acquired in the StripMap mode, and thus, both the azimuth and ground range resolutions were about 3.3 m. The images were orthorectified multi-look corrected products (EEC) where the image distortion caused by a variable terrain height was compensated using SRTM/DEM, a globally available digital elevation model. The images were then resampled and overlaid on a WGS84 reference ellipsoid with a square pixel size of 1.25 m.

Two preprocessing approaches were applied to the images before extracting flooded areas and damaged buildings. First, the three TSX images were transformed to a sigma naught (σ^0) value, which represents the radar reflectivity per unit area in the ground range. After the transformation, the backscattering coefficients of the images became between –30 dB and 30 dB. Then, an enhanced Lee filter (Lopes et al. 1990) was applied to the SAR data to reduce speckle noise. To minimize the loss of information contained in the SAR intensity images, the window size of the filter was set as 3×3 pixels.

CRUSTAL MOVEMENTS IN THE TOHOKU EARTHQUAKE

Since the TSX images used in this study were geo-coded by the GPS orbit determination with a high level of accuracy (Breit et al. 2010), the displacements between the pre- and post-event TSX images were mostly caused by crustal movements due to the earthquake. A color
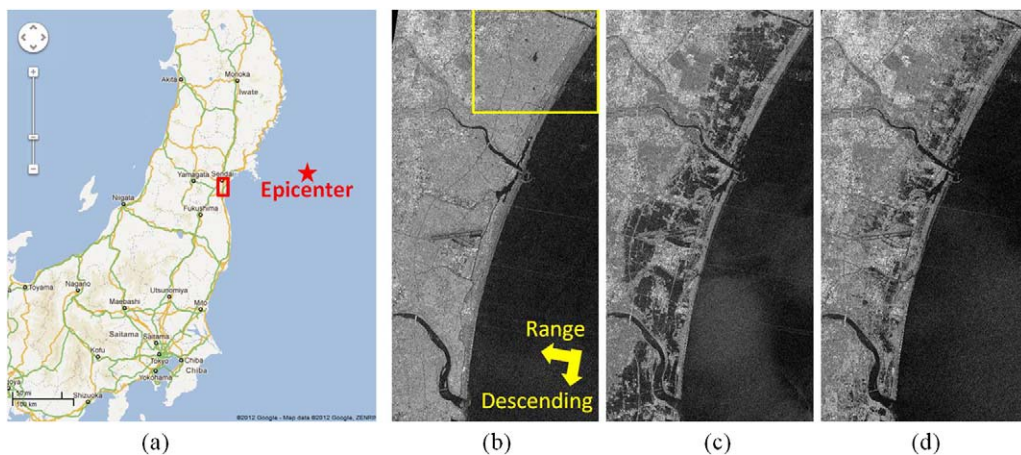

Figure 1. (a) Study area along the Pacific coast of Sendai, Japan; (b) the pre-event TSX image taken on 21 October 2010; and (c) the post-event images taken on 13 March 2011 and (d) on 24 March 2011.
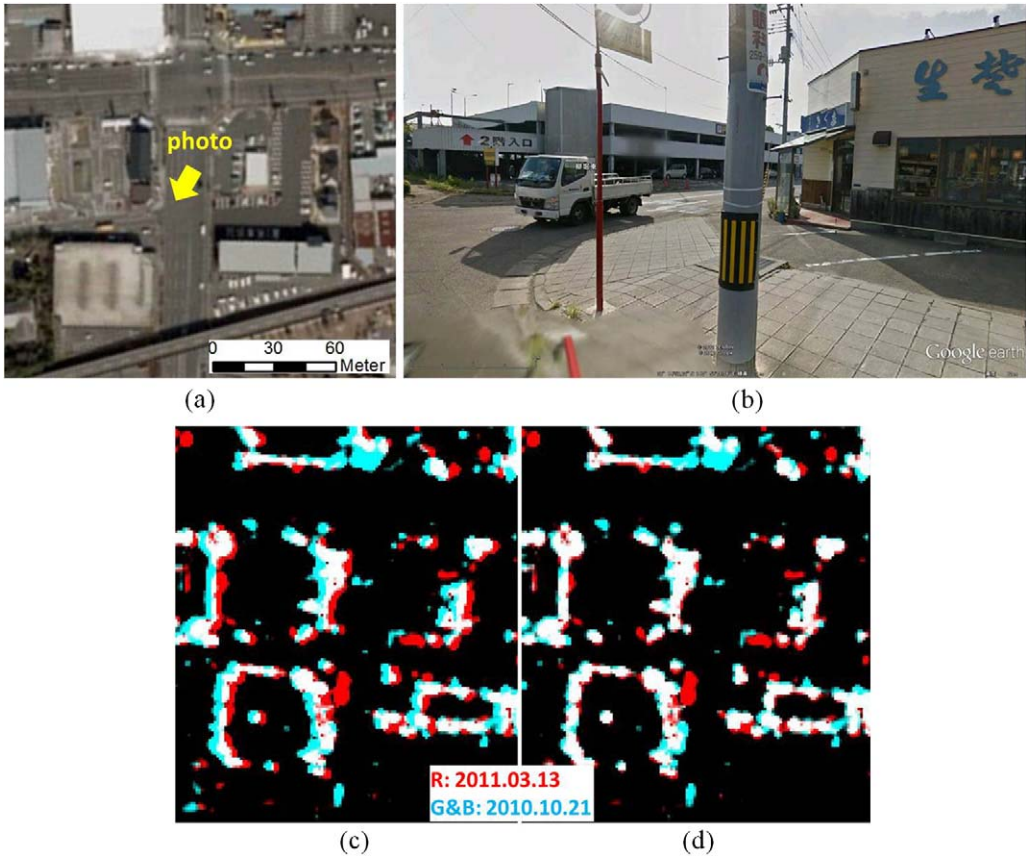
Figure 2. (a) Aerial photographs taken on 24 March 2011 and (b) street view obtained from Google Earth; (c) the color composite of the original pre- and post-event (13 March) TSX intensity images with displacement due to the crustal movement; and (d) the shifted pre- and post-event composite image without displacement.

composite image is shown in Figure 2c, where the pre-event images were loaded as green and blue while the post-event image on 13 March 2011 as red. The outlines of buildings in Figure 2a are seen to be shifted from cyan to red. From the ground photo shown in Figure 2b, it can be confirmed that the buildings were not damaged during the earthquake. These displacements were used to detect crustal movements (Liu and Yamazaki 2012), but caused errors when detecting changes associated with flooded areas and damaged buildings in this study. As an approach for emergency response, the pre- and post-event images were shifted manually in the pixel unit to be registered in this study. According to the records from Natori GPS ground station in the study area, 3.18 m southeast horizontal and 0.25 m downward movements were observed until 13 March 2011 as shown in Figure 3. Since the area surrounding the Natori station was severely affected by tsunamis, the GPS station stopped operation until 18 April 2011.
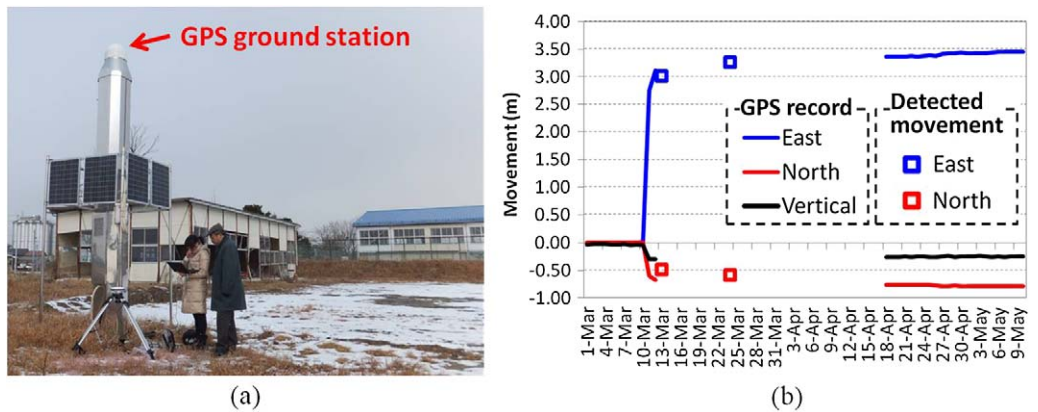
Figure 3. (a) Photograph of field survey at Natori GPS station taken on 13 January 2012; (b) the observed 3-D movements at Natori station from 1 March to 25 April 2011, where the reference value (zero) is data for 21 October 2010.

The displacements caused by the crustal movements when the post-event TSX images were taken were estimated by Liu and Yamazaki (2013). The three-dimensional (3-D) surface displacements recorded at the GPS station were converted to two-dimensional displacements in the TSX images, considering the side-looking observation mode of SAR. The movement detected in the TSX image on 13 March was 3.11 m to the east and 0.55 m to the south while that on 24 March was 3.22 m to the east and 0.59 m to the south. Considering that the displacements obtained by Liu and Yamazaki (2013) were approximately 0.3 m larger than the GPS data, the post-event TSX images were shifted manually by 2 pixels (2.5 m) to the west (to the left as viewed by an on-screen user) in order to match with the pre-event TSX image; the two temporal shapes of buildings were then almost overlapped in the new color composite, shown in Figure 2d.

EXTRACTION OF FLOODED AREAS

The color composite of the three processed TSX images is shown in Figure 4a. According to recent studies, water surface shows the lowest backscatter compared with other forms of land cover; thus, flooded areas can easily be seen in the color composite image. The areas that were flooded on 13 March but above water on 24 March are shown in purple (R+B) while the areas still flooded on 24 March are shown in blue. Since the study area is flat with urban and agricultural use, the analysis suggests that the tsunami penetrated approximately 4 km inland from the coastline. Many rice paddies remained flooded for a few months after the main shock due to the influence of land subsidence resulting from the crustal movement.

METHODOLOGY

The difference in backscattering coefficients between the pre- and post-event SAR images is the simplest and most efficient index to identify flooded areas. Due to the decrease in backscattering coefficients caused by flooding, subtracting the pre-event value from the post-event one gives a negative value for flooded areas. However, if the difference is
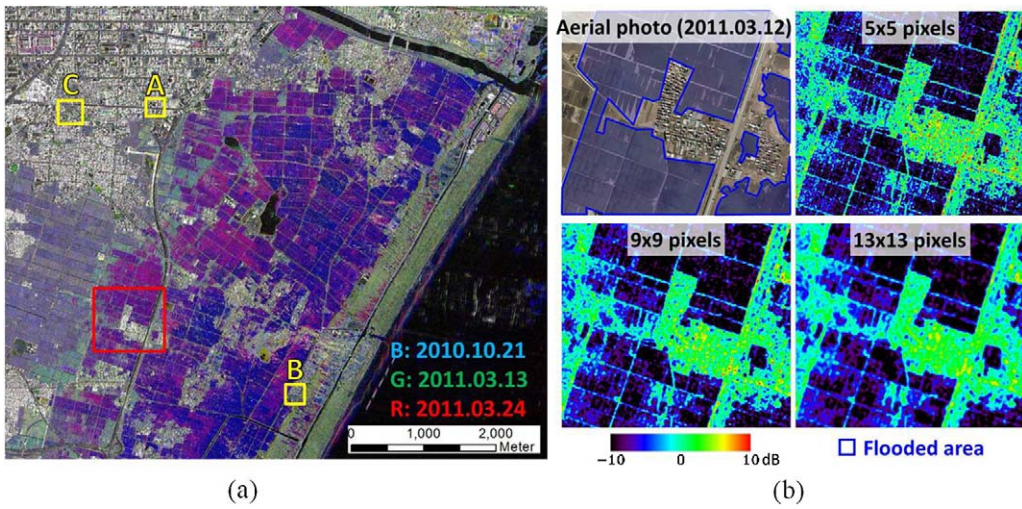
Figure 4. (a) The color composite of three temporal TSX intensity images; (b) comparison of aerial photographs over the area in the red square of (a), and the differences between the pre- and post-event (13 March) TSX images calculated by window sizes of 5 × 5, 9 × 9, and 13 × 13 pixels.

calculated directly, pixel by pixel, noise might be included due to high sensitivity of the X-band SAR. Thus, an average-difference method was used in this study.

A small window was selected for the pre- and post-event TSX images of the same location. The difference between the two average backscatter values in the window was calculated at the center pixel of the window. This method smoothed differences and reduced the residual errors caused by crustal movements. The window ranged in size from 3 × 3 to 15 × 15 pixels. As the window size became larger, the difference value became smoother.

The results with different window sizes (5 × 5, 9 × 9, and 13 × 13 pixels) are shown in Figure 4b. Compared with the aerial photographs taken on 12 March 2011, the boundaries of the flooded areas could be correctly extracted in most areas when the window size was 9 × 9 pixels (about 14 m × 14 m). When the window size was set as 5 × 5 pixels, the changes associated with damaged buildings remained and were mistakenly extracted as flooded areas. When the window size was set as 13 × 13 pixels, the boundaries of flooded areas became too vague. Hence, we found that the 9 × 9 window as the most appropriate size to extract flooded areas, and was applied to all the TSX images thereafter.

The threshold value (T) of the backscatter intensity to extract flooded areas was determined by two different methods, and termed as T_1 and T_2, respectively. Firstly, T_1 was calculated by Equation 1 using the average value (μ) and standard deviation (σ) of the histogram. The average value of the difference between the pre-event image and the post-event image on 13 March 2011 was –1.49 dB, and the standard deviation was 4.97 dB; Equation 1 then gave a T_1 value of –6.46 dB.

$$T_1 = \mu - \sigma \tag{1}$$

Secondly, T_2 was calculated by Otsu (1979) method, a method for automatic histogram-based image threshholding. Otsu's method is based on the idea of finding the threshold that minimizes the weighted within-class variance as the same as maximizing the between-class variance. According to the histogram of the difference image, T_2 was –4.75 dB. Since T_2 was greater than T_1, larger areas were categorized as being flooded. Comparing the two threshold values visually, T_1 was seen to be more suitable. The areas with difference less than –6.46 dB between the pre-event and first post-event images were extracted as flooded on 13 March 2011. Since the average of difference from the 24 March image was –0.56 dB and the standard deviation value was 3.83 dB, the threshold value for 24 March was –4.75 dB. However, the threshold value for the 13 March image was more suitable for flood extraction according to the visual comparison. The microwave shooting condition for the image on 24 March was similar to that on 13 March, and thus the same threshold value –6.46 dB was also used to extract the flooded areas on 24 March.

IMAGE ANALYSIS

After extracting flooded areas using the averaged difference, three approaches were applied to improve the accuracy of the initial result. The first method was to fill holes that were caused by debris in the extracted areas. Since the flooded areas were extracted by the decrease in the backscattering coefficient, the pixel values in flooded areas with floating debris did not decrease, or even increased, and thus, such pixels could not be extracted. As such, this step categorized pixels as flooded if completely surrounded by flooded areas. Then errors were removed.

In addition to the areas flooded by tsunamis, there were many other reductions of backscatter due to demolition of buildings and relocation of vehicles. These changed areas were much smaller than the flooded areas. Since most of the flooded areas were paddy fields forming blocks larger than 300 m^2, the extracted areas covering less than 200 pixels (about 312 m^2) were removed from the result.

Finally, existing water bodies from the pre-event time were accounted for. Since the X-band SAR is sensitive to small changes, the backscatter from river and other water surfaces varies according to wave (wind) conditions. These changes were not caused by tsunamis and were therefore removed from the extracted result. Thus, the original water bodies with backscatter coefficient less than –10.0 dB were extracted from the pre-event SAR image. The detected water areas were smooth, as shown in Figure 5a. After removing the original water areas, the extracted flooded areas are shown in Figure 5b. The extracted result from the TSX image taken on 13 March was assigned as red, and the result extracted from the 24 March image was assigned as green plus blue (cyan). The white pixels shown in Figure 5b were then considered as the flooded areas until 24 March, and the red pixels were those on 13 March but dried on Mach 24. There are several cyan pixels near the river in Figure 5b, which are the areas with newly decreased values after 13 March 2011, mainly caused by removal of debris or vegetation.

The run-up measurements by PASCO Corporation (2011) were used to verify our results, as shown by the yellow lines in Figure 5. The run-up boundary was extracted from several high-resolution optical (RapidEye and WoldView) and SAR (TerraSAR-X, PALSAR) images. Since the areas most severely affected by the tsunami were still flooded on
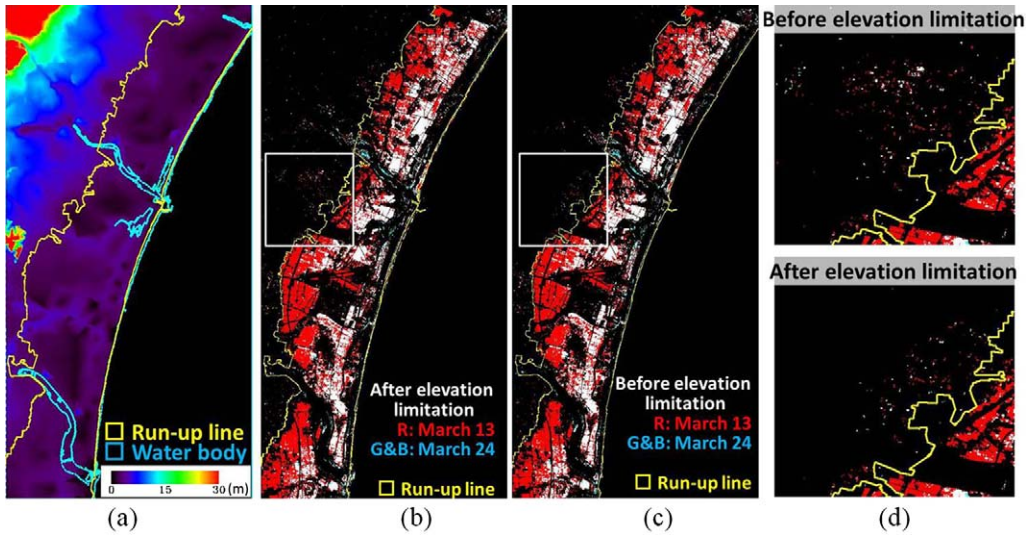
Figure 5. (a) Original water body obtained from the pre-event TSX image overlapping on the 10 m digital elevation model (DEM) from GSI; (b and c) comparison of the extracted flooded areas on 13 March and 24 2011 with the run-up boundary from PASCO, before and after introducing the elevation limit; and (d) close-up of the area in the white frame.

13 March 2011, the boundary of the extracted result was close to the run-up boundary determined by PASCO. Compared with the optical image, the extraction errors outside the run-up boundary were caused by the changes of buildings. Although these errors were reduced by setting a size-limit threshold, the changes of large buildings located in spacious grounds still remained in the result.

RELATIONSHIP BETWEEN FLOODED AREAS AND ELEVATION

The 5 m and 10 m mesh DEMs produced by GSI were used to investigate the relationship between the flooded areas and their elevations. The 10 m DEM was produced from the contours of a 1:25,000 topographic map and covers most areas of Japan. The 5 m DEM was obtained from Aerial Laser Scanner and only covers several major cities in Japan. According to the 10 m DEM shown in Figure 5a, the study area is basically flat, without much relief. While highest elevation is 124 m, but 99% of the total area is at elevations of less than 6 m. Overlaying the extracted result on the DEM showed that 99% of the extracted flooded areas were below 4 m. Hence, any extracted areas higher than 4 m were removed from the result as errors. After introducing this elevation limit, the extracted result shown in Figure 5c showed higher coincidence with the run-up boundary.

The accuracy of our extracted result on 13 March 2011 was examined using the run-up boundary by PASCO Corp. as a reference. The target area covers about 1083 km^2, and 109.7 km^2 areas were within the run-up boundary. The proposed method extracted 46.2 km^2 as flooded areas on 13 March. The overall accuracy for flooded areas was 79.1% while the user accuracy was 98.9%, and the producer accuracy was 40.6%. Here, user accuracy refers to the probability that a pixel classified as a particular habitat on the

image is actually that habitat, and the producer accuracy refers to the probability that a pixel in a given habitat category will have been classified correctly on the image. Comparing with the result without elevation limit shown in Figure 5b, the overall accuracy and the user accuracy has increased about 1%. A pick-up comparison of the results before and after introducing elevation limit was shown in Figure 5d, where the areas located at high elevations, and thus not flooded, could be removed. The producer accuracy of our result is low because of affected buildings, debris, and original water bodies within the inundation zone, below the maximum run-up line. Although the individual buildings within the flooded areas could be extracted as flooded correctly by closing holes within the flooded areas, the flooded built-up areas could not be extracted as flooded areas due to the reflection of buildings. It should be noted that, since flat areas, such as the runway in Sendai Airport, had low backscatter prior to the earthquake, they could not be extracted after flooding. However, the high user accuracy shows that the extracted flooded areas were almost all located within the inundation zone.

Compared with the 3 m resolution TSX images, the 10 m DEM looks too coarse to investigate the elevation limit of tsunami flooding. Therefore, the 5 m DEM around Sendai City, shown in Figure 6a, was employed in this study. From Figure 6a, small reliefs, such as a hill and an expressway, are clearly visible in the 5 m DEM. The histogram of the elevation with respect to the PASCO's run-up boundary and our extracted result is shown in Figure 6b in a 1 m elevation increment. Since the tsunami, with more than a 10 m height, hit the study area, the run-up boundary extends to the areas of 10 m in elevation. However, the flooded areas on 13 March were all below 3 m, and 98% were located below 2 m.

DETECTION OF DAMAGED BUILDINGS

Numerous buildings were demolished and washed away by the huge tsunami of more than 10 m, and hence, it was difficult to observe damaged buildings individually during field surveys, due to widespread destruction. The proposed method was tested regarding whether it
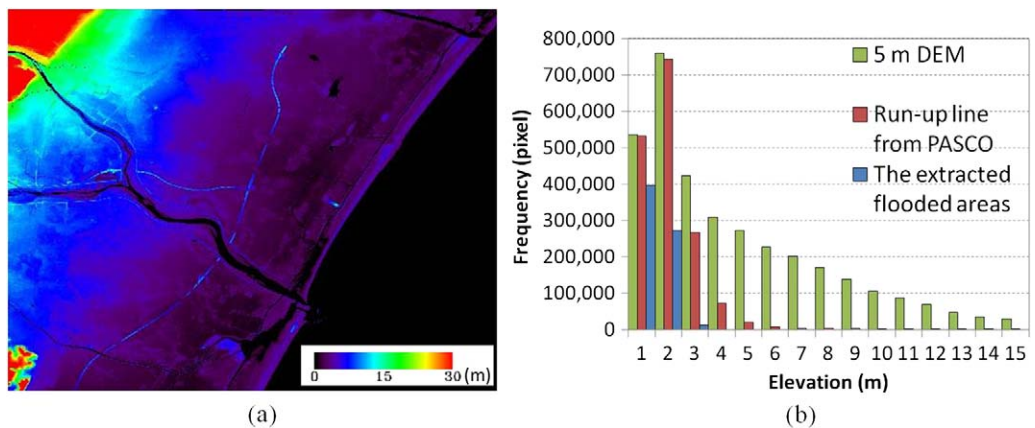

Figure 6. (a) The 5 m digital elevation model from GSI near Sendai City; (b) the histogram of the elevation where less than 15 m, the elevation of the PASCO run-up boundary and that of the extracted flooded areas in this study, which shows the elevation of flooded areas are lower than the run-up line.
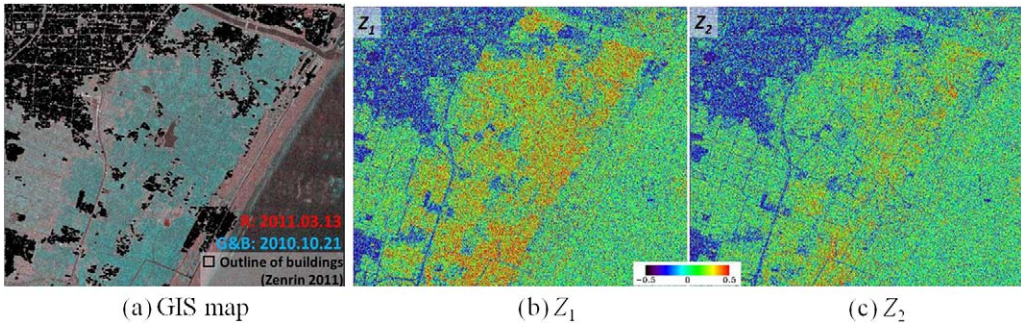
(a) GIS map   (b) Z_1 (c) Z_2

Figure 7. (a) A GIS map of buildings over the color composite of the pre- and post-event TSX images; (b) the change factor calculated from the pre-event image and the image taken on 13 March 2011; and (c) the image taken on 24 March 2011, in which the red indicates high probability of change.

can extract damage for each building unit, using the high-resolution pre- and post-event TSX intensity images and a GIS map of buildings produced by Gokon and Koshimura (2012), shown in Figure 7a.

CALCULATION OF A CHANGE FACTOR

The backscattering coefficients for damaged buildings can both increase and decrease, depending on the severity of damage. Additionally, the backscattering coefficients for no-change (undamaged) buildings have very high correlation between the pre- and post-event TSX images. Hence, we took advantage of these features to detect damaged buildings using a change factor that includes both the difference and correlation coefficient (Liu and Yamazaki 2011). The change factor between the pre-event image and the post-event image on 13 March 2011 is termed z_1, while that between the pre-event image and the image on 24 March 2011 is termed z_2. The two change factors were calculated by Equation 2 and are shown in Figure 7b–c:

$$z = \left| \frac{d}{\max|d|} \right| - c \cdot r \tag{2}$$

where

$$r = \frac{N \sum\limits_{i=1}^{N} Ia_i Ib_i - \sum\limits_{i=1}^{N} Ia_i \sum\limits_{i=1}^{N} Ib_i}{\sqrt{\left(N \sum\limits_{i=1}^{N} Ia_i^2 - \left(\sum\limits_{i=1}^{N} Ia_i \right)^2 \right)} \sqrt{\left(N \sum\limits_{i=1}^{N} Ib_i^2 - \left(\sum\limits_{i=1}^{N} Ib_i \right)^2 \right)}}, \tag{3}$$

where $\max(|d|)$ is the maximum absolute value of the difference of the backscattering coefficients; c is the weight between the difference and the correlation coefficient, to be

determined between 0.0 and 1.0; Ia_i and Ib_i are the backscattering coefficients of the i-th pixel of the pre- and post-event images; and N $(= k \times k)$ is the window size.

The window size to detect damaged buildings was set as 5×5 pixels (about 40 m^2) due to the smaller scale of a single building compared with a flooded paddy field. Since the correlation coefficient is very sensitive to subtle changes, it showed a low value even when no large change had occurred. Conversely, the normalized absolute value of the difference was relatively stable. Hence, in this study, the weight for the correlation coefficient was set as half of that for the correlation, which is 0.5. It means the change in difference is counted more than that in correlation. As a result, the theoretical value of the z-factor lies between –0.5 and 1.5, where a high value indicates high probability of change. In Figure 7(b–c), the z_1 is between –0.5 and 1.3 while the z_2 is between –0.5 and 1.2. The change factors for flooded coastal areas are highest, displayed in red, while the factors for northwestern urban areas are lowest, displayed in blue. The highest change factor occurs in the area where a building was completed wash away and became a water area on 13 March.

BUILDING DAMAGE DETECTION

Building damage can be detected by the amount of change in a building's outline. The data of building outlines was cited from *Zenrin Product 2011*, which was made by visual interpretation using aerial photographs taken before 2010 (Zenrin 2011). However, the outlines of buildings in the GIS map did not match those in the TSX images, due to the side-looking nature of SAR. A building in a TSX image shows layover from the actual position to the direction of the sensor, as shown in Figure 8a. The layover is proportional to the building height, as in Equation 4:

$$L = H/\tan \theta \tag{4}$$

where θ is the incident angle of the microwave.
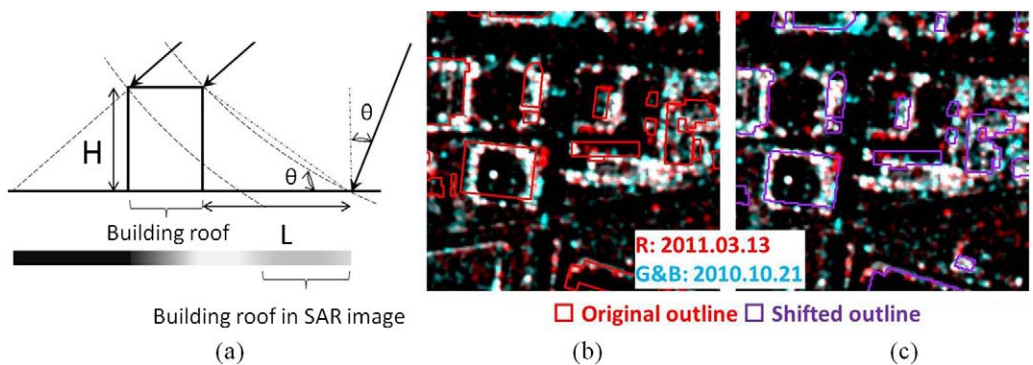

Figure 8. (a) Simulation of the location of a building in a SAR image; (b) close-up of the area A in Figure 4 (the same area with Figure 2) with the original building outline; and (c) the modified result after shifting the GIS map.

Figure 8b shows the outlines of buildings over the color composite of the pre- and post-event (13 March 2011) images. The walls of a building, which show highest backscatter due to corner reflection, are outside the outline in the GIS map. In this case, the building cannot be detected as damaged even when a large change occurs to its walls. Therefore, the GIS map was shifted to the direction of the SAR sensor (southeast) in order to match with the TSX images. Since the height data for buildings was not available, all the buildings in the study area were considered as two-storied with a 6 m height. The layover was then approximately 7.9 m, as calculated from the 37.3° incidence angle. The path of TSX was 190.4° clockwise from the north, which means that the layover can be decomposed into 7.8 m to the east and 1.4 m to the south. Hence, the GIS map was shifted 6 pixels to the east and 2 pixels to the south. The new building outlines, after shifting, were plotted on the TSX color composite image in Figure 8c. Compared with Figure 8b, larger areas of high backscattering intensities were located within the building outlines.

A building with an average factor value greater than 0 within its outline is considered as damaged. A part of buildings categorized as damaged are shown in Figure 9a–b, using the change factors for 13 March and 24 March 2011, respectively. Comparison with the aerial photographs taken before and after the earthquake, shown in Figure 9c–d, confirmed that buildings that were completely washed away were detected successfully using the both factors. However, some extensively damaged buildings where debris remained at the same position could not be detected by z_1 for the 13 March 2011 image, due to the small change in backscatter. From the TSX image taken on 24 March 2011, some of these buildings became distinguishable due to the ongoing removal of debris. Thus, both the z_1 and z_2 factors were used to detect damaged buildings in this study. A building was classified as damaged if the averaged value for either factor was greater than 0. The results are shown in Figure 10a.

MODIFICATION AND VERIFICATION

Comparing the detected damaged buildings in Figure 10a with the extracted flooded areas in the previous section, several damaged buildings were located outside the flooded areas; one example is shown in Figure 11a. Aerial photographs taken before and after the earth-quake over the same location are shown in Figure 11b–c. From the aerial photographs,
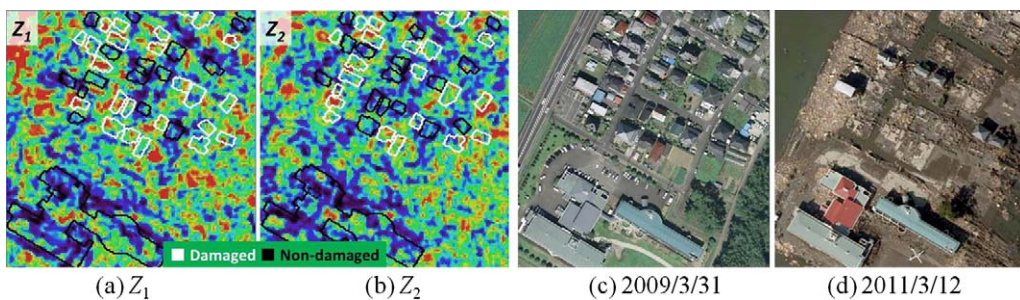

(a) Z_1 (b) Z_2 (c) 2009/3/31   (d) 2011/3/12

Figure 9. The result obtained using factors (a) z_1 and (b) z_2 of the area B in Figure 4; (c) aerial photograph taken on 31 March 2009, cited from Google Earth; and (d) image acquired on March 12 2011 by GSI.
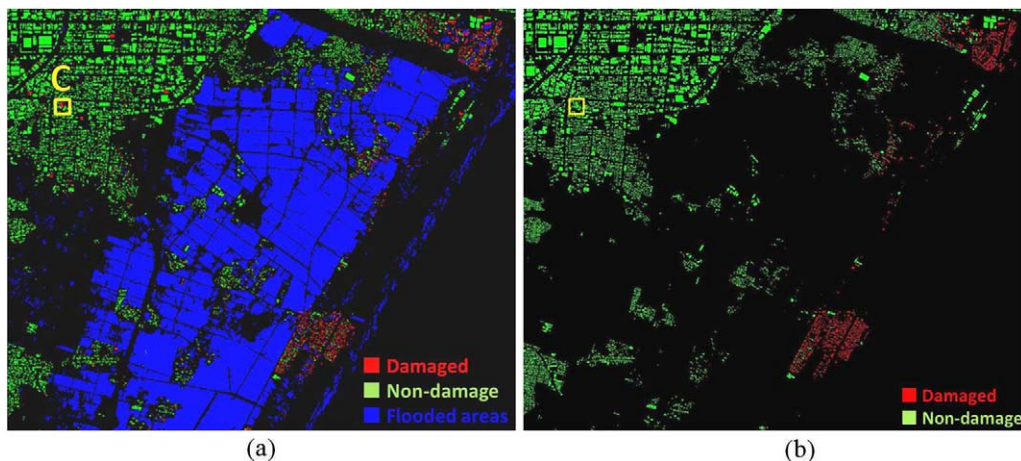
Figure 10. The damaged buildings extracted using both (a) z_1 and z_2; and (b) a modified result by introducing the limit of the flooded areas (b).
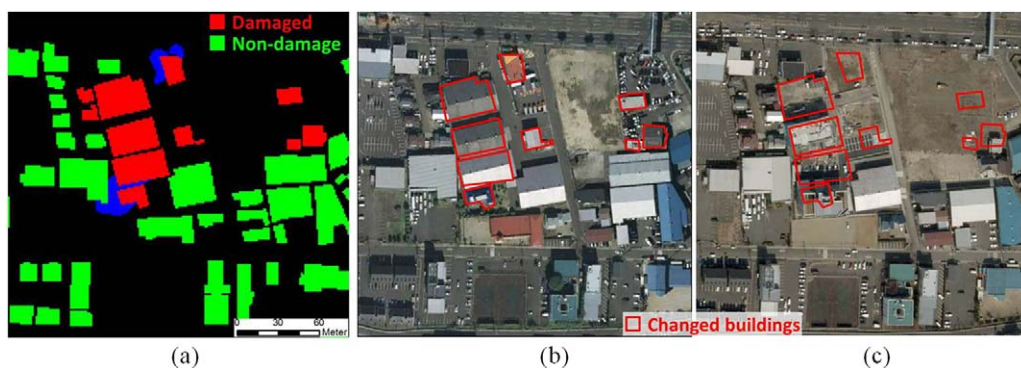

Figure 11. (a) Close-up of the area C in Figure 10a; (b and c) aerial photographs taken on April 4, 2010 and 24 March 2011.

it could be confirmed that ten neighboring buildings were rebuilt at the same time, which led them to be mistakenly classified as damaged buildings. Additionally, three adjacent buildings were extracted as a flooded area because they presented a relatively large block of decreased backscatter.

The introduction of the limit of inundation, which we also refer to as the run-up boundary, is the most efficient means to remove these errors from calculation. However, this study used the extracted flooded areas in order to test its usefulness whenever no validated ground measurements exist, and thus check whether it may be useful for rapid damage assessment in areas when ground teams have not yet entered. Since the Pacific Ocean coastline is located in

the east of the TSX images, damaged buildings located at the outside-west of the flooded areas were removed as errors. Although the extracted flooded areas had high user accuracy, errors still remained, as shown in Figure 11a. Thus, flooded areas less than 20 pixels (25 m) wide were considered as invalid. The modified result is shown in Figure 10b, in which errors in the western urban areas had been removed.

To verify the accuracy of our estimates, the building damage map produced by Gokon and Koshimura (2012), shown in Figure 12, was used as a reference. The building map was made by visual interpretation using the post-event aerial imagery and the building outlines provided by Zenrin Co. There are approximately 45,000 buildings in the study area; the pixel-based accuracy is shown in Table 1a while the building unit-based accuracy is shown in Table 1b. When the result was evaluated by pixel-base, the overall accuracy of damaged buildings was 95%, with producer accuracy of 82% and user accuracy of 71%. When the result was evaluated by building unit-base, the overall accuracy was 94%, producer accuracy was 79%, and user accuracy was 74%. When evaluated by building-unit, the reduced accuracy was caused by classification errors for small buildings.

There are two reasons for classification errors in the detection process. The first is the discrepancy between the real locations of buildings and those in the TSX images. Since all the buildings in the study area were assumed to be 6 m high, the outlines of one-storied or three-storied buildings were not matched with those in the TSX images. Thus, some damaged buildings of these types could not be detected. Additionally, some undamaged buildings
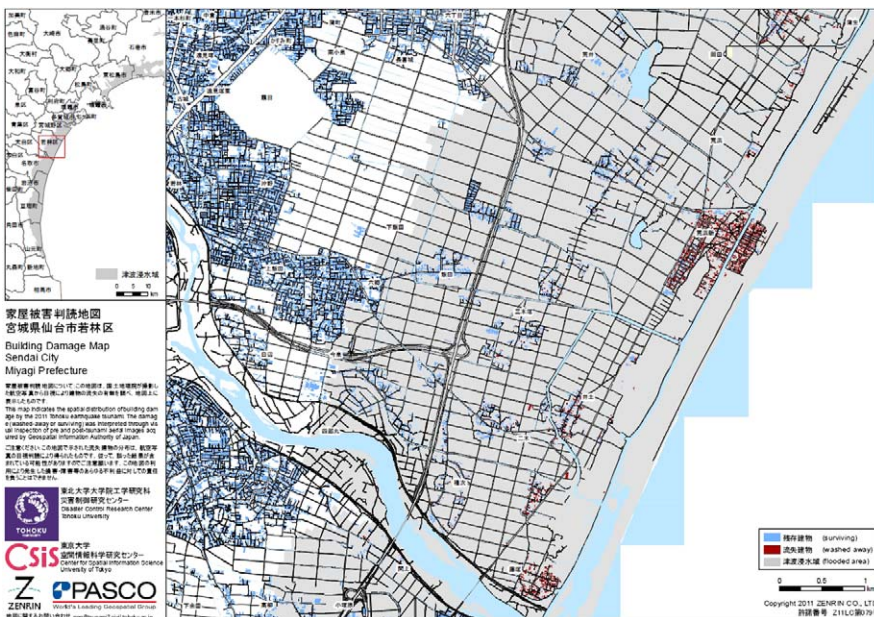

Figure 12. Building damage map of Sendai City produced by Gokon and Koshimura (2012) using GIS data and aerial photographs taken after the earthquake, where washed-away buildings are in red and surviving buildings in cyan.

Table 1. Accuracy of damage detection evaluated by (a) pixel-based and (b) building unit–based methods

(a)

		Building damage map by Gokon and Koshimura (%)			
		Washed away	Survived	Total	User Accuracy
Detected result	Damaged	7.6	3.1	10.7	70.6
	No damage	1.6	87.7	89.3	97.0
	Total	9.2	90.8	100.0	-
	Producer accuracy	82.2	96.5	-	95.2

(b)

		Building damage map by Gokon and Koshimura (building unit)			
		Washed away	Survived	Total	User Accuracy (%)
Detected result	Damaged	4,309	1,496	5,805	74.2
	No damage	1,163	37,627	38,790	97.0
	Total	5,472	39,123	44,595	–
	Producer accuracy (%)	78.7	96.2	–	94.0

located within the flooded areas were misclassified as damaged. The second reason is the influence of debris. As shown in Figure 9, some washed-away buildings with debris left at the original locations could not be detected correctly.

CONCLUSIONS

In this study, the damage following the 2011 Tohoku-oki earthquake and tsunami in Sendai was assessed using high-resolution TerraSAR-X intensity images taken before and after the earthquake. From the pre- and post-event backscattering coefficient images, flooded areas were extracted reliably, due to a drastic decrease of backscatter. The most appropriate sizes for the smoothing window and the backscattering difference threshold were assessed by comparison with aerial photographs. The run-up boundary from PASCO was used as a reference to verify the accuracy of flooded-area extraction. Although not all the flooded areas were extracted, the user accuracy was about 99% after introducing the elevation limitation. However, the accuracy of flooded extraction by the proposed method will decrease when applied to built-up areas. A digital elevation model by GSI was also introduced to investigate the relationship between flooded areas and elevation. Although the tsunami intruded into the areas of 10 m elevation, the flooded areas at the time of SAR data acquisitions were all located below 2 m elevation.

Damaged and washed-away buildings were detected individually from the changes of backscattering coefficients. The average value for the change factors in the outline of each building was calculated and used to judge the damage status of the building. The resulting classifications were compared with a GIS damage map produced by visual interpretation, showing that the proposed method achieved more than 90% overall accuracy.

According to these results, the proposed approach, which uses only high-resolution SAR images, is considered reliable to use in emergency response planning following natural disasters. There are two parameters used in the proposed method for each detection: the window size and the threshold value. The window size depends on the spatial resolution of an image and the size of targets. Although the threshold value for flooded-area extraction was defined by visual comparison, the threshold value, which is set as 0 for the change factor, can be seen as fixed. Thus, the proposed method can be applied easily to wide areas in less time and with less labor compared with visual interpretation. However, the proposed method can be applied only on the temporal SAR images with the same incident angle. Additionally, high-resolution optical images will be necessary to build building outlines in case no GIS data is available.

Since the pre- and post-event TSX images were registered roughly, the accuracy of results can be improved with finer registration. The accuracy is also considered to depend on the spatial resolution; therefore the application of higher-resolution TSX images, such as HighSpot mode, can improve the result, especially for the detection of damaged buildings. Additionally, available height information of buildings from a 3-D GIS can also improve the outline expansion process and the result of detection. A part of the proposed method for damaged buildings will be improved in the near future by accounting for the different heights of buildings, which can be detected from a pre-event SAR image. It is also expected that the damage status can be classified into finer classes using the change factors.

ACKNOWLEDGEMENTS

REFERENCES

Ahton, P., Euro, M., Hallikainen, M., Solbø, S., Johansen, B., and Solheim, I., 2004. *SAR and Optical Based Algorithms for Estimation of Water Bodies*, Technical Report, FloodMan Project.

Brunner, D., Lemoine, G., and Bruzzone, L., 2010. Earthquake damage assessment of buildings using VHR optical and SAR imagery, *IEEE Transactions on Geoscience and Remote Sensing* **48**, 2403–2420.

Dell'Acqua, F., and Gamba, P., 2012. Remote sensing and earthquake damage assessment experiences, limits, and perspectives, *Proceedings of the IEEE* **100**, 2876–2890.

Dellepiane, S., Bo, G., Monni, S., and Buck, C., 2000. SAR images and interferometric coherence for flood monitoring, *Proceedings of International Geoscience and Remote Sensing Symposium* **XI**, 2608–2610.

Geist, E. L., Titov, V. V., and Synolakis, C. E., 2006. Tsunami: wave of change, *Scientific American*, 56–63.

Geudtner, D., Winter, R., and Vachon, P., 1996. Flood monitoring using ESR-1 SAR interferometry coherence maps, *Proceedings of International Geoscience and Remote Sensing Symposium* **II**, 966–968.

Geospatial Information Authority of Japan (GSI), 2011. http://www.gsi.go.jp/BOUSAI/h23_tohoku.html.

Gokon, H., and Koshimura, S., 2012. Mapping of building damage of the 2011 Tohoku Earthquake Tsunami in Miyagi prefecture, *Coastal Engineering Journal* **54**, 1250010-1–1250010-25.

Fritz, H. M., Philips, D. A, Okayasu, A., Shinozono, T., Liu, H., Mohammed, F., Skanavis, V., Synolaks, C. E., and Takehashi, T. 2012. The 2011 Japan tsunami current velocity measurements from survivor videos at Kesennuma Bay using LIDAR, *Geophysical Research Letters* **39**, L00G23.

Horritt, M. S., 1999. A statistical active contour model for SAR image segmentation, *Image and Vision Computing* **17**, 213–224.

Heremans, R., Willekens, A., Borghys, D., Verbeeck, B., Valckenborg, J., Acheroy, M., and Perneel, C., 2003. Automatic detection of flooded areas on ENVISAT/ASAR images using an object-oriented classification technique and an active contour algorithm, *Proceedings of IEEE Conference on Recent Advances in Space Technologies*, 289–294.

Ito, Y., Hosokawa, M., Lee, H., and Liu, J.G., 2000. Extraction of damaged regions using SAR data and neural networks, ISPRS2000, *International Activities of Photogrammetry and Remote Sensing* **XXXIII**, Part B1, 156–163.

Lopes, A., Touzi, R., and Nezry, E., 1990. Adaptive speckle filters and scene heterogeneity, *IEEE Transactions on Geoscience and Remote Sensing* **28**, 992–1000.

Liu, W., and Yamazaki, F., 2011. Urban change monitoring by from multi-temporal TerraSAR-X images, *Joint Urban Remote Sensing Event*, 277–280.

Liu, W., and Yamazaki, F., 2013. Detection of Crustal Movement from TerraSAR-X intensity images for the 2011 Tohoku, Japan Earthquake, *Geoscience and Remote Sensing Letters* **10**, 199–203, doi: 10.1109/LGRS.2012.2199076.

Matsuoka, M., and Yamazaki, F., 2004. Use of satellite SAR intensity imagery for detection building areas damage due to earthquake, *Earthquake Spectra* **20**, 975–994.

Matsuoka, M., and Yamazaki, F., 2005. Building damage mapping of the 2003 Bam, Iran, Earthquake using Envisat/ASAR intensity imagery, *Earthquake Spectra* **21**, S285–S294.

Matgen, P., Schumann, G., Henry, J.-B., Hoffmann, L., and Pfister, L., 2007. Integration of SAR-derived inundation areas, high precision topographic data, and a river flow model toward real-time flood management, *Journal of Applied Earth Observation and Geoinformation* **9**, 247–263.

Mitsoudis, D. A., Flouri, E. T., Chrysoulakis, N., Kamarianakis, Y., Okal, E. A., and Synolakis, C.E., 2012. Tsunami hazard in the southeast Aegean Sea, Costal Engineering **60**, 136–148.

Otsu, N., 1979. A threshold selection method from gray-level histograms, *IEEE Transactions on Systems, Man, and Cybernetics* **SMC-9**, 62–66.

PASCO Corporation, 2011. http://www.pasco.co.jp/disaster_info/110311/.

Wang, T. L., and Jin, Y. Q., 2012. Postearthquake building damage assessment using multi-mutual information from pre-event optical image and postevent SAR image, *IEEE Geoscience and Remote Sensing Letters* **9**, 452–456.

Yonezawa, C., and Takeuchi, S., 2001. Decorrelation of SAR data by urban damages caused by the 1995 Hyogoken-Nanbu earthquake, *International Journal of Remote Sensing* **22**, 1585–1600.

Zenrin, 2011. http://www.zenrin.co.jp/.